Supporting information

Stress-relieving Carboxylated Polythiophene/Single-Walled Carbon Nanotube Conductive Layer for Stable Silicon Microparticle Anodes in Lithium-Ion Batteries

Donghee Gueon[a‡], Haoze Ren[a‡], Zeyuan Sun[a], Bar Mosevitzky Lis[a], Dang D. Nguyen[a], Esther S. Takeuchi[b,c,d,e], Amy C. Marschilok[b,c,d,e], Kenneth J. Takeuchi[b,c,d,e], Elsa Reichmanis*[a]

[a] Department of Chemical and Bimolecular Engineering, Lehigh University, Bethlehem, PA, 18015, United States

[b] Interdisciplinary Science Department, Brookhaven National Laboratory, Upton, New York, 11973, United States

[c] Institute of Energy: Sustainability, Environment and Equity, Stony Brook University, Stony Brook, New York, 11794, United States

[d] Department of Material Science and Chemical Engineering, Stony Brook University, Stony Brook, New York, 11794, United States

[e] Department of Chemistry, Stony Brook University, Stony Brook, New York, 11794, United States

*Corresponding Author: Elsa Reichmanis, elr420@lehigh.edu

‡D.G and H.R contributed equally to this paper.

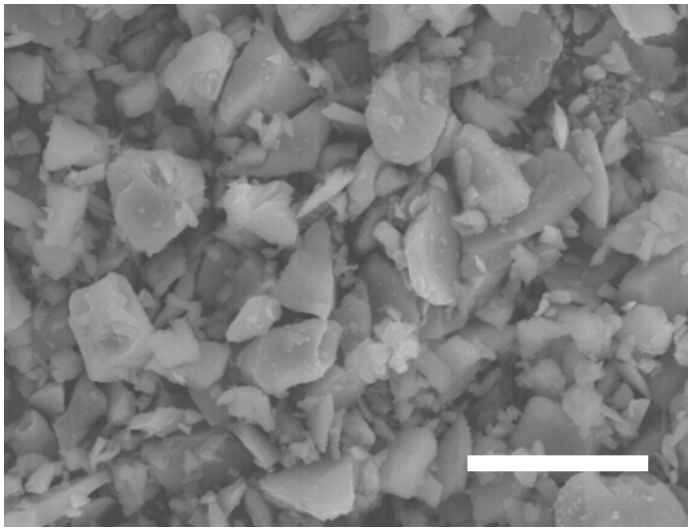

Figure S1. SEM image of silicon micro-particles (Si MPs). (Scale bar: 10 μm)

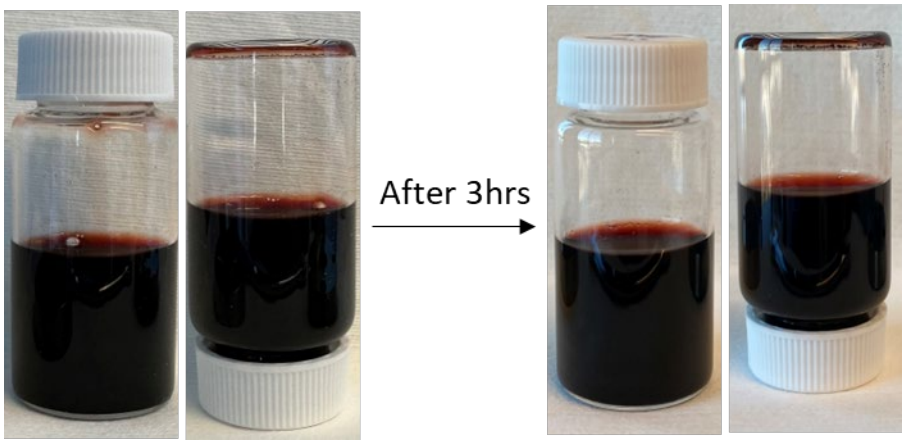

Figure S2. Well dispersed poly[3-(potassium-4-butanoate)thiophene]/ single-walled carbon nanotubes (PPBT/SWNT).

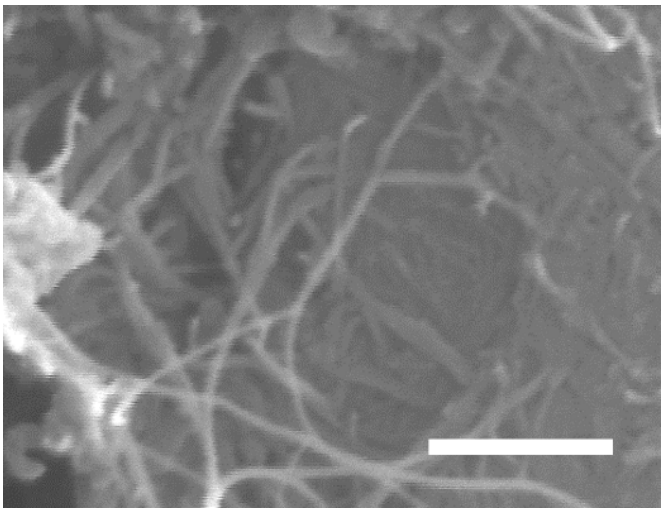

Figure S3. SEM image of PPBT/SWNT powder. (Scale bar: 200 nm)

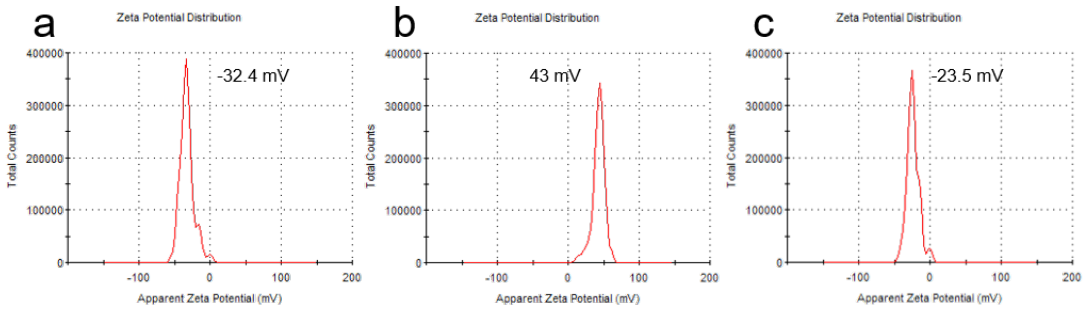

Figure S4. Zeta potential distributions of (a) Si MPs, (b) Poly (diallydimethylammonium chloride) pretreated Si MPs, and (c) PPBT/SWNT@Si MPs.

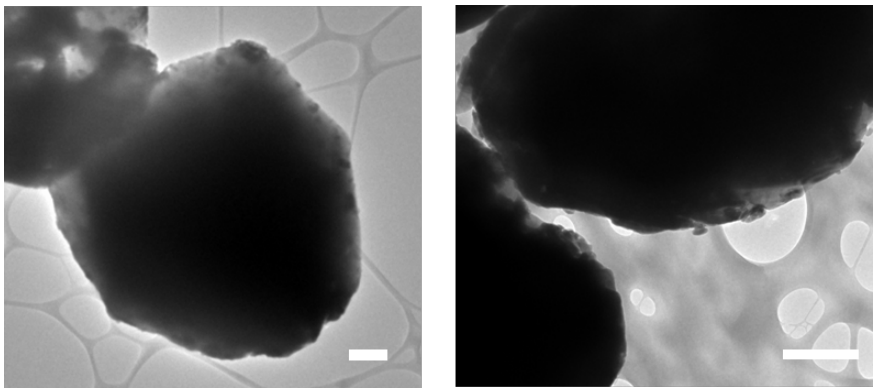

Figure S5. Transmission electron microscopy (TEM) images of Si MPs. (Scale bar: 500 nm)

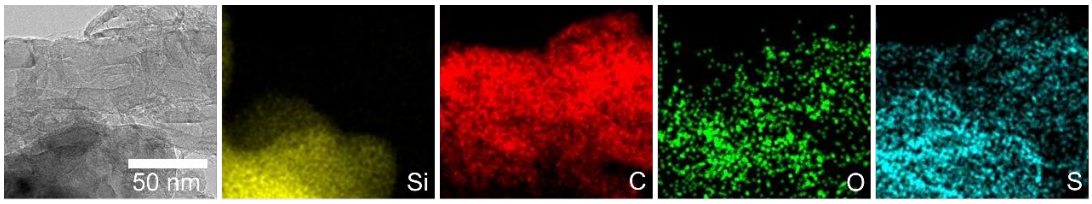

Figure S6. TEM images of PPBT/SWNT@Si MPs and the Energy Dispersive Spectroscopy (EDS) mapping images.

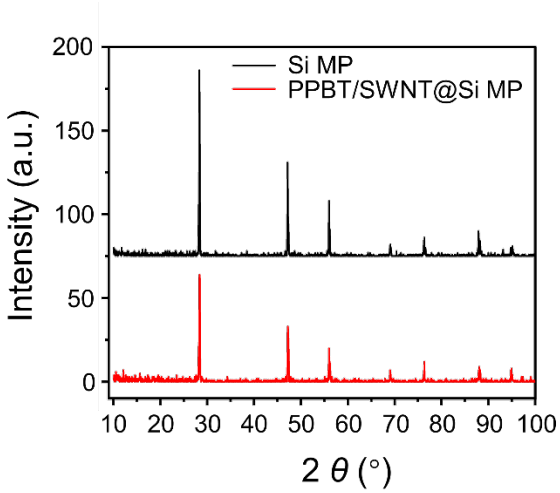

Figure S7. X-Ray diffraction analysis pattern of Si MP and PPBT/SWNT@Si MP.

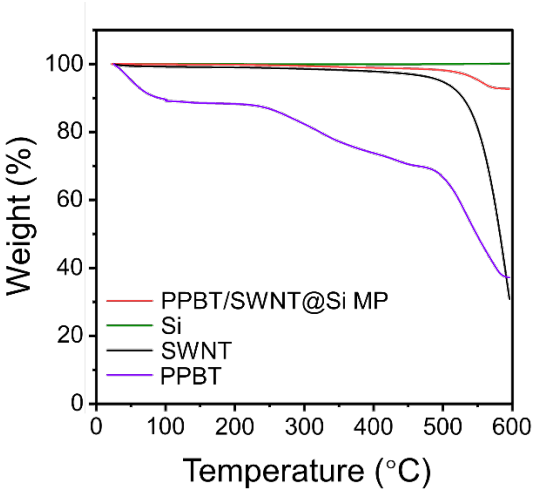

Figure S8. TGA profile. The TGA tests were carried out in air in the temperature range of 25-600 °C at a heating rate of 10 °C/min.

Table S1. material weight before and after the TGA test.

Material	Before TGA	After TGA	Mass residual ratio
PPBT/SWNT@Si MPs	14.33 mg	13.29 mg	92.72 %
Si MPs	20.82 mg	20.85 mg	100.15 %
PPBT	6.73 mg	2.50 mg	37.21 %
SWNT	6.11 mg	1.88 mg	30.86 %

Calculation:

In PPBT/SWNT@Si MPs before TGA analysis, the Si MP weight is $x\ mg$, the SWNT weight is $\frac{x*0.01}{0.27}\ mg$, and the PPBT weight is $y\ mg$.

Based on the TGA data the following equation can be obtained:

$$x + \frac{x*0.01}{0.27} + y = 14.33 \quad (\textbf{Equation S1})$$

$$x * 100.15\% + \frac{x*0.01}{0.27} * 30.86\% + y * 37.21\% = 13.29 \quad (\textbf{Equation S2})$$

The Si MP weight in PPBT/SWNT@Si MPs can be calculated based on the previous two equations. Then, the weight ratio of Si MPs in PPBT/SWNT@Si MPs can be calculated based on $\frac{x}{14.33} * 100\% \approx 88.6\%$

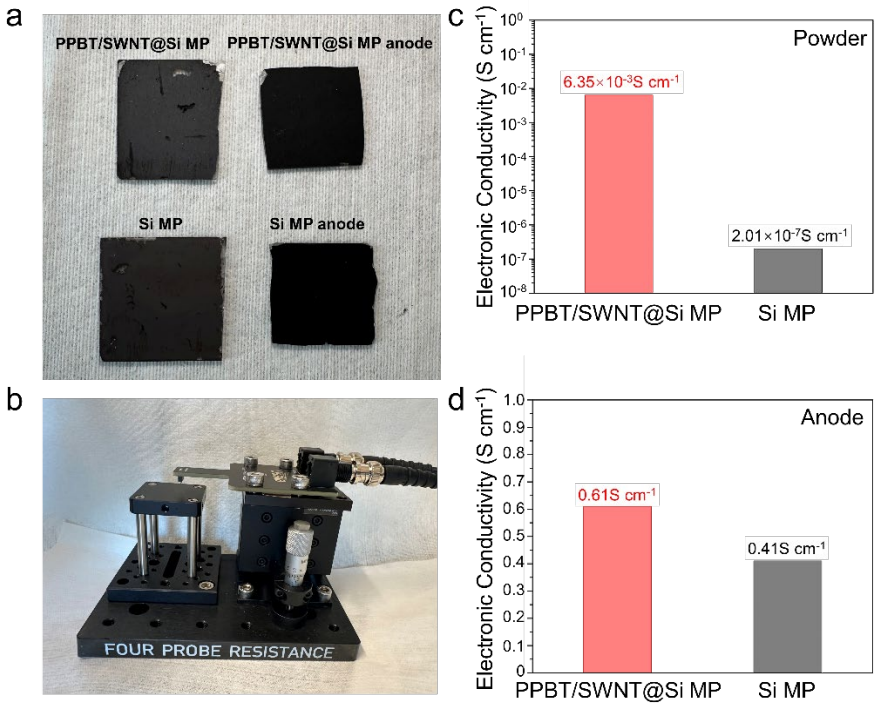

Figure S9. (a) Digital image of PPBT/SWNT@Si MPs and Si MPs, and the related anodes coated on glass substrate. (b) 4-point probe test equipment. (c) Electronic conductivity of PPBT/SWNT@Si MP and Si MP. (d) Electronic conductivity of PPBT/SWNT@Si MP and Si MP anodes.

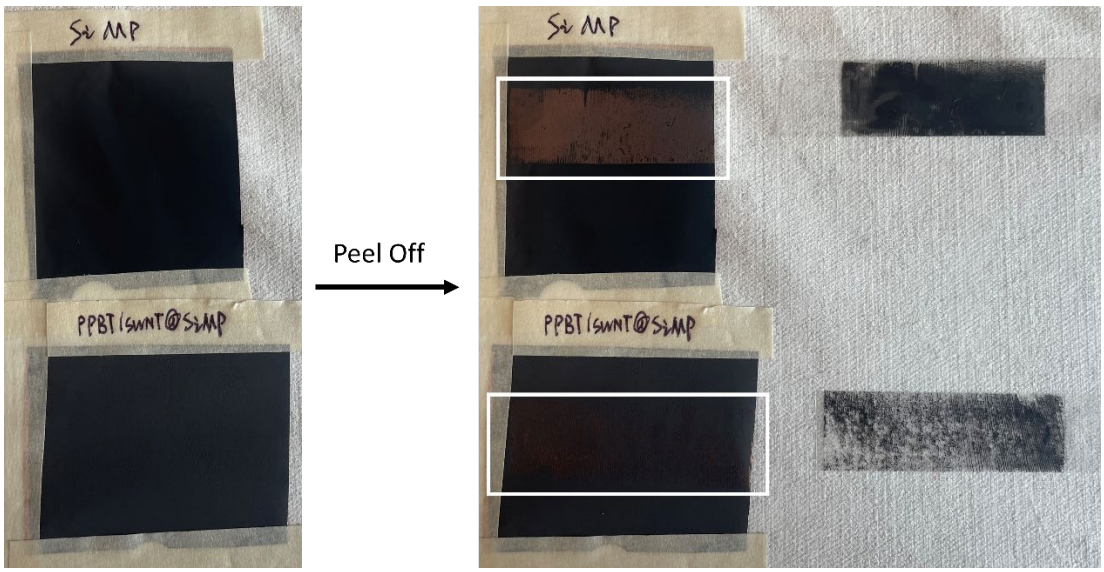

Figure S10. Electrode peel-off experiment for both Si MP and PPBT/SWNT@Si MP anode.

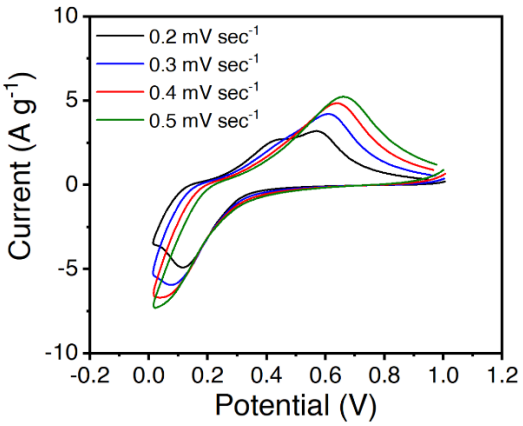

Figure S11. Oxidation/reduction voltage profiles of Si MP anodes at a various scan rate from 0.2 to 0.5 mV s^{-1}.

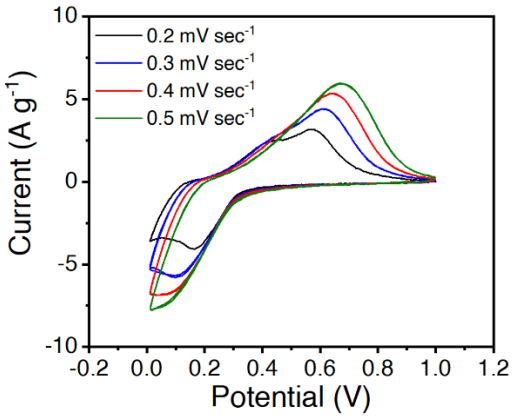

Figure S12. Oxidation/reduction voltage profiles of PPBT/SWNT@Si MP anodes at a various scan rate from 0.2 mV s^{-1} to 0.5 mV s^{-1}.

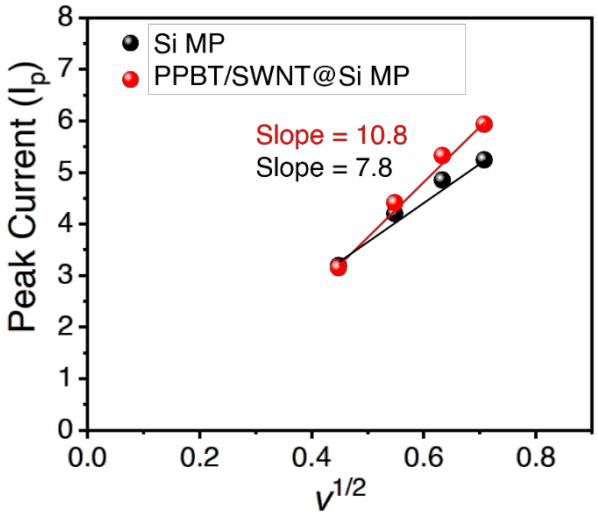

Figure S13. The relationship of peak current and the square root of scan rate ($v^{1/2}$) for anodic peaks of Si MP and PPBT/SWNT@Si MP anodes.

Table S2. Comparison of ICE of previously reported Si-based anodes.

Materials	ICE (%)	Binder	Reference
Si/mesoporous carbon/crystalline TiO_2 nanoparticles	73 %	PAA	1
Carbon-coated ant-nest-like microscale porous silicon	80.3 %	Sodium alginate	2
Si/Ti_3C_2 Mxene composite	61.1 %	PVDF	3
3D N-doped graphene@Si@Hybrid Silicate	74.9 %	/	4
MXene-Si-CNT composite	70.38 %	CMC	5
Carbon-coated metallurgical Silicon/carbon nanofiber	73 %	Sodium alginate	6
poly(hexaazatrinaphthalene) coated Si/C microsized particles	81.29 %	Sodium alginate	7
Microclusters of kinked silicon nanowires	82.4 %	PAA	8
Nano Si	81.6%	Self-healing polymer binder	9
PPBT@CNT/Si MPs	85 %	PAA/PVA	This work

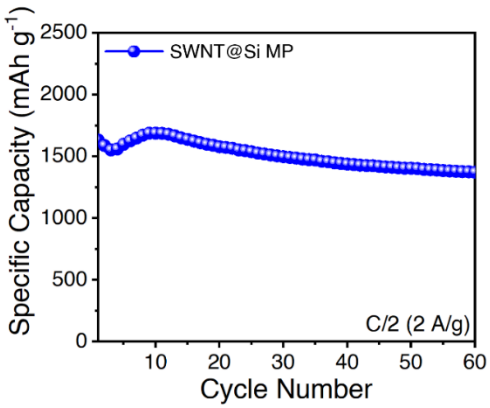

Figure S14. SWNT@Si MP anodes cycle performance at a current density of 2 A g^{-1}.

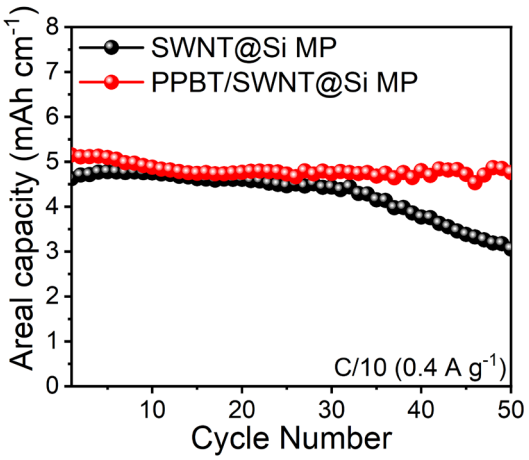

Figure S15. High mass loading (~ 2mg cm^{-2}) PPBT/SWNT@Si MP and SWNT@Si MP anodes cycle performance at a current density of 0.4 A g^{-1}.

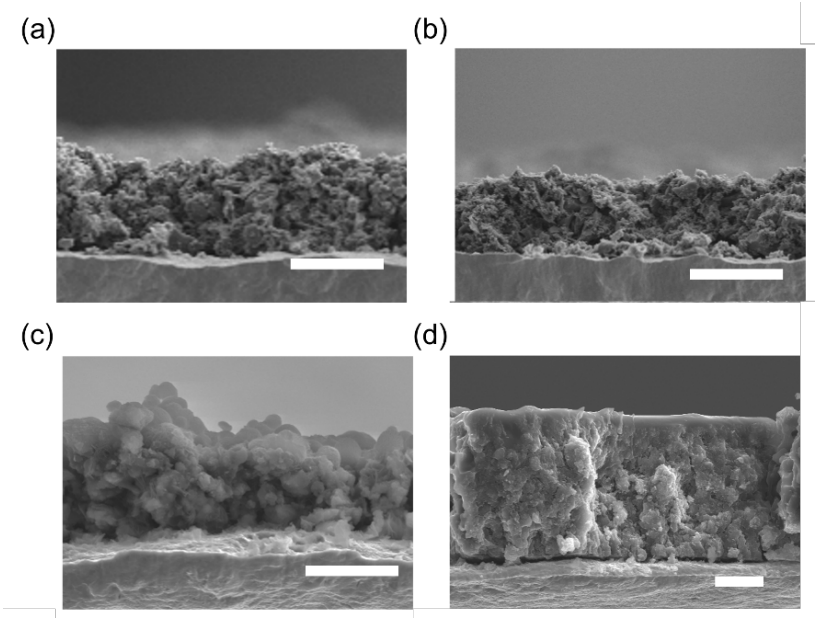

Figure S16. Cross-sectional image of PPBT/SWNT@Si MP and Si MP anode (a, b) before and (c, d) after cycling. (Scale bar: 10 μm)

Table S3. Comparison of the initial capacity and capacity decay rate of previously reported nano-silicon anodes.

Materials / **Binders**	**Current Rate/ Density**	**Initial Capacity (mAh/g)**	**Capacity decay rate (%)**	**Reference**
Si nanoparticle/ double carbon matrix / PAA	0.2 C	≈1500	0.040 %	[10]
Si nanoparticle/ zeolite imidazolate frameworks / PVDF	1A/g	≈2800	≈0.084 %	[11]
Si nanoparticle / PVDF/ self-healing poly(ether-thioureas)	4.2 A/g	≈1016	0.058 %	[12]
Si nanoparticle/ 50 nm void mesoporous yolk-shell carbon / CMC	0.42 A/g	1272	0.054 %	[13]
Si nanotube / Sodium alginate	1 A/g	2197	0.047 %	[14]
Si nanosheet / CMC/SBR	2 A/g	≈2000	0.050 %	[15]
Si nanoparticle/ hollow porous carbon/ graphene / CMC	0.1 A/g	1556	0.165 %	[16]
Silicon particle / PAA/gelatin/β-cyclodextrin cross-link polymer	2 A/g	2461	0.13%	[17]
Si microparticle/ PPBT/SWNT / PAA/PVA	2 A/g	2063	0.027 %	This work

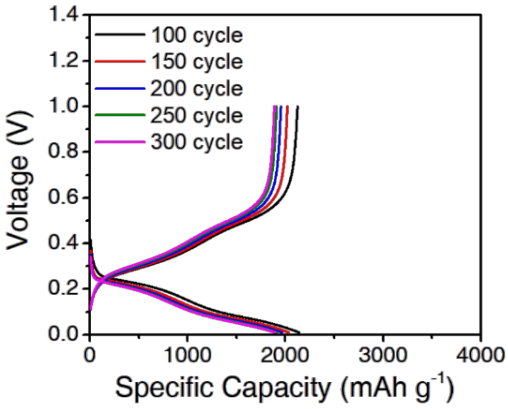

Figure S17. Charge/discharge voltage profiles of PPBT/SWNT@Si MPs at a current density of 2 A g-1 for 300 cycles.

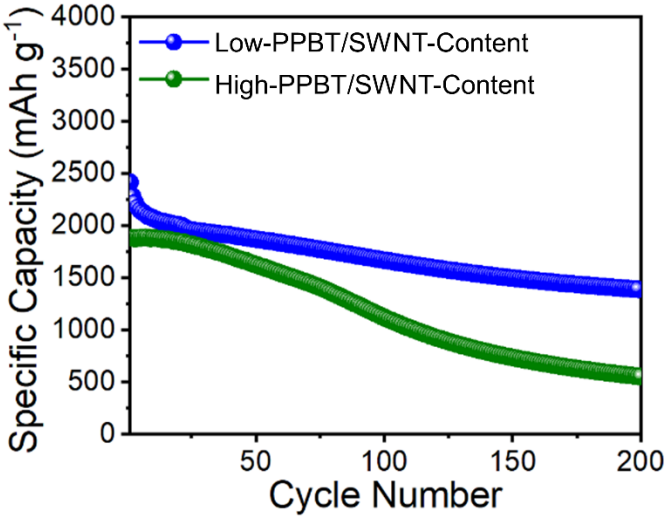

Figure S18. Cycle performance of PPBT/SWNT@Si MP anodes with different PPBT/SWNT content.

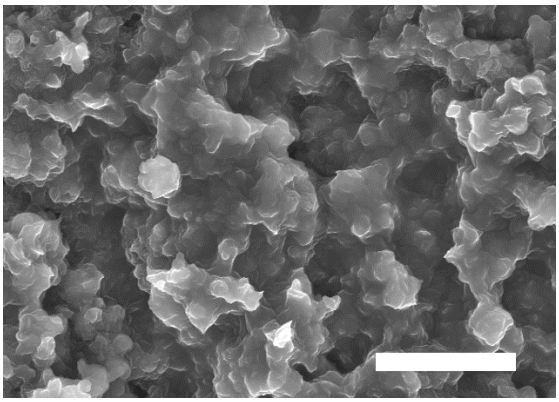

Figure S19. SEM images of higher PPBT/SWNT Si MP anode after cycling. (Scale bar: 10 μm)

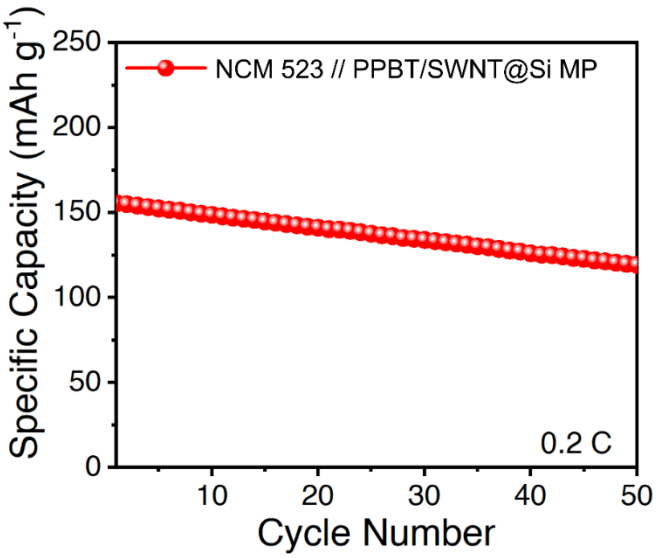

Figure S20. Cycle performance of NCM 523 // PPBT/SWNT@Si MP electrodes based full cell at 0.2 C.

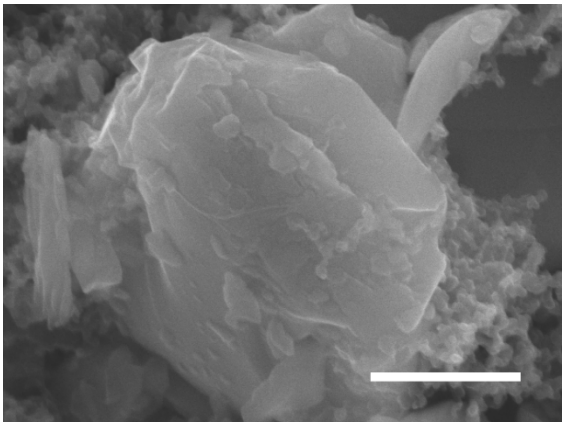

Figure S21. SEM image of SWNT/Si MP anodes. (Scale bar: 1 μm)

The Raman shifts are converted to the strain on carbon nanotubes according to the equation below:

$$\Delta G = G - G_{OCV} - G \quad \text{(Equation S3)}$$

Where G_{OCV} is the G-band position at open circuit voltage, and G is the G-band position during cycling.

$$F = -\frac{\Delta G}{8} \times 1.1\ TPa \times 1\% \quad \text{(Equation S4)}$$

where ΔG is the G-band shifts, and F is the strain on SWNT.

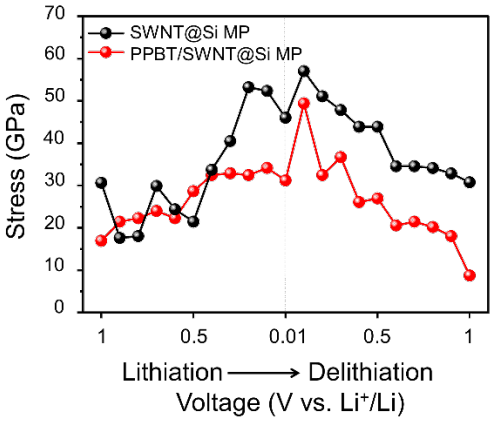

Figure S22. The corresponding stress for the SWNTs in the PPBT/SWNT@Si MP and SWNT@Si MP anodes during the 2nd cycle.

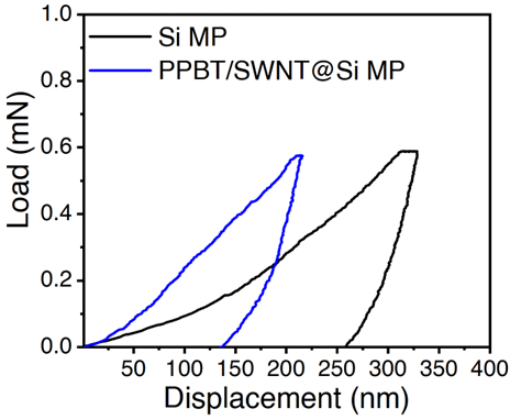

Figure S23. load-depth profiles of Si MP and PPBT/SWNT@Si MP electrodes with a maximum load of 0.6 mN.

REFERENCES

1. Luo, W.; Wang, Y.; Wang, L.; Jiang, W.; Chou, S.-L.; Dou, S. X.; Liu, H. K.; Yang, J., Silicon/mesoporous carbon/crystalline TiO2 nanoparticles for highly stable lithium storage. *ACS Nano* **2016,** *10* (11), 10524-10532.

2. An, W.; Gao, B.; Mei, S.; Xiang, B.; Fu, J.; Wang, L.; Zhang, Q.; Chu, P. K.; Huo, K., Scalable synthesis of ant-nest-like bulk porous silicon for high-performance lithium-ion battery anodes. *Nat. Commun.* **2019,** *10* (1), 1447.

3. Hui, X.; Zhao, R.; Zhang, P.; Li, C.; Wang, C.; Yin, L., Low-temperature reduction strategy synthesized Si/Ti3C2 MXene composite anodes for high-performance Li-ion batteries. *Adv. Energy Mater.* **2019,** *9* (33), 1901065.

4. Huang, G.; Han, J.; Lu, Z.; Wei, D.; Kashani, H.; Watanabe, K.; Chen, M., Ultrastable silicon anode by three-dimensional nanoarchitecture design. *ACS Nano* **2020,** *14* (4), 4374-4382.

5. Liu, S.; Zhang, X.; Yan, P.; Cheng, R.; Tang, Y.; Cui, M.; Wang, B.; Zhang, L.; Wang, X.; Jiang, Y., Dual bond enhanced multidimensional

constructed composite silicon anode for high-performance lithium ion batteries. *ACS Nano* **2019,** *13* (8), 8854-8864.
6. Shen, C.; Fang, X.; Ge, M.; Zhang, A.; Liu, Y.; Ma, Y.; Mecklenburg, M.; Nie, X.; Zhou, C., Hierarchical carbon-coated ball-milled silicon: synthesis and applications in free-standing electrodes and high-voltage full lithium-ion batteries. *ACS Nano* **2018,** *12* (6), 6280-6291.
7. Wang, Q.; Zhu, M.; Chen, G.; Dudko, N.; Li, Y.; Liu, H.; Shi, L.; Wu, G.; Zhang, D., High-performance microsized Si anodes for lithium-ion batteries: insights into the polymer configuration conversion mechanism. *Adv. Mater.* **2022,** *34* (16), 2109658.
8. Jeong, Y. K.; Huang, W.; Vilá, R. A.; Huang, W.; Wang, J.; Kim, S. C.; Kim, Y. S.; Zhao, J.; Cui, Y., Microclusters of kinked silicon nanowires synthesized by a recyclable iodide process for high-performance lithium-ion battery anodes. *Adv. Energy Mater.* **2020,** *10* (41), 2002108.
9. Li, Z.; Wan, Z.; Zeng, X.; Zhang, S.; Yan, L.; Ji, J.; Wang, H.; Ma, Q.; Liu, T.; Lin, Z.; Ling, M.; Liang, C., A robust network binder via localized linking by small molecules for high-areal-capacity silicon anodes in lithium-ion batteries. *Nano Energy* **2021,** *79*, 105430.
10. Kwon, H. J.; Hwang, J. Y.; Shin, H. J.; Jeong, M. G.; Chung, K. Y.; Sun, Y. K.; Jung, H. G., Nano/Microstructured Silicon-Carbon Hybrid Composite Particles Fabricated with Corn Starch Biowaste as Anode Materials for Li-Ion Batteries. *Nano Lett* **2020,** *20* (1), 625-635.
11. Gao, R.; Tang, J.; Yu, X.; Tang, S.; Ozawa, K.; Sasaki, T.; Qin, L.-C., In situ synthesis of MOF-derived carbon shells for silicon anode with improved lithium-ion storage. *Nano Energy* **2020,** *70*, 104444.
12. Chen, H.; Wu, Z.; Su, Z.; Chen, S.; Yan, C.; Al-Mamun, M.; Tang, Y.; Zhang, S., A mechanically robust self-healing binder for silicon anode in lithium ion batteries. *Nano Energy* **2021,** *81*, 105654.
13. Yang, J.; Wang, Y.-X.; Chou, S.-L.; Zhang, R.; Xu, Y.; Fan, J.; Zhang, W.-x.; Kun Liu, H.; Zhao, D.; Xue Dou, S., Yolk-shell silicon-mesoporous carbon anode with compact solid electrolyte interphase film for superior lithium-ion batteries. *Nano Energy* **2015,** *18*, 133-142.
14. Wang, F.; Li, P.; Li, W.; Wang, D., Electrochemical Synthesis of Multidimensional Nanostructured Silicon as a Negative Electrode Material for Lithium-Ion Battery. *ACS Nano* **2022,** *16* (5), 7689-7700.
15. Ren, Y.; Xiang, L.; Yin, X.; Xiao, R.; Zuo, P.; Gao, Y.; Yin, G.; Du, C., Ultrathin Si Nanosheets Dispersed in Graphene Matrix Enable Stable Interface and High Rate Capability of Anode for Lithium-ion Batteries. *Adv. Funct. Mater.* **2022,** *32* (16), 2110046.
16. Chen, H.; He, S.; Hou, X.; Wang, S.; Chen, F.; Qin, H.; Xia, Y.; Zhou, G., Nano-Si/C microsphere with hollow double spherical interlayer and submicron porous structure to enhance performance for lithium-ion battery anode. *Electrochimica Acta* **2019,** *312*, 242-250.

17. Ye, R.; Liu, J.; Tian, J.; Deng, Y.; Yang, X.; Chen, Q.; Zhang, P.; Zhao, J., Novel Binder with Cross-Linking Reconfiguration Functionality for Silicon Anodes of Lithium-Ion Batteries. *ACS Appl Mater Interfaces* **2024,** *16* (13), 16820-16829.